Int. J. Solids Structures Vol. 23, No. 7, pp. 1063–1085, 1987
Printed in Great Britain.

0020–7683/87 $3.00+ .00

NECKING AND NECK PROPAGATION IN POLYMERIC MATERIALS UNDER PLANE-STRAIN TENSION

P. Tuğcu and K. W. Neale
Faculty of Applied Sciences, Université de Sherbrooke, Sherbrooke, Québec, Canada J1K 2R1

(*Received* 26 *May* 1986; *in revised form* 14 *October* 1986)

Abstract—Necking and neck propagation as observed in cold-drawing polymers is analysed for plane-strain tensile loading. Approximate one- and two-dimensional analyses are presented for quasi-static neck propagation along an infinitely long specimen. In addition, the entire load–deformation behaviour of finite length specimens is computed using the finite element method. Various material models describing effects such as rate dependence and anisotropic (kinematic) hardening are considered.

1. INTRODUCTION

Many polymers, when loaded in tension, behave in the manner displayed in Fig. 1. Necking initially develops in the specimen as the load–elongation curve reaches a maximum, and then localizes under decreasing load. As loading progresses this localization eventually ceases and further loading forces the neck to propagate along the specimen. The regions through which the neck has spread exhibit stiffnesses and hardnesses significantly superior to those possessed by the polymer in its initial state. This process, termed "cold drawing", is exploited in the commercial production of hard polymeric fibres and films and is thus of considerable practical interest.

Although cold drawing has been observed for many years, the mechanical aspects of neck propagation have only recently been fully elucidated. Coleman (1983) has conducted an analysis for steady-state neck propagation, but within the framework of the one-dimensional equilibrium theory of bars. Hutchinson and Neale (1983) have presented both simple one-dimensional analyses as well as an approximate three-dimensional analysis for axisymmetric neck propagation along cylindrical round bars. In a subsequent study, Neale and Tuğcu (1985) have carried out a full three-dimensional finite element analysis for the entire load–deformation behaviour of a round tensile specimen. Neck propagation under plane-strain deformations has been considered by Fager and Bassani (1984).

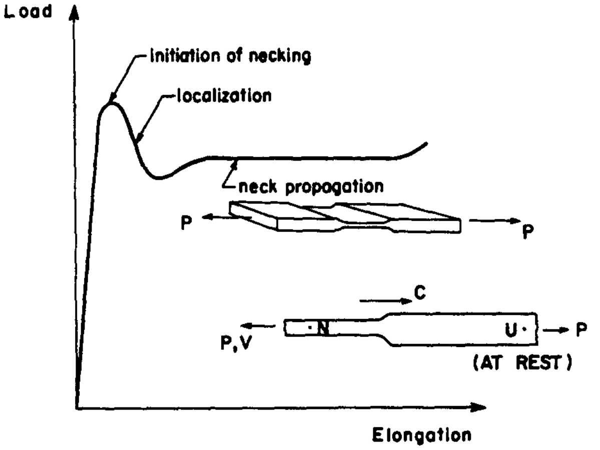

Fig. 1. Load–elongation behaviour for a cold-drawing polymer in plane-strain tension.

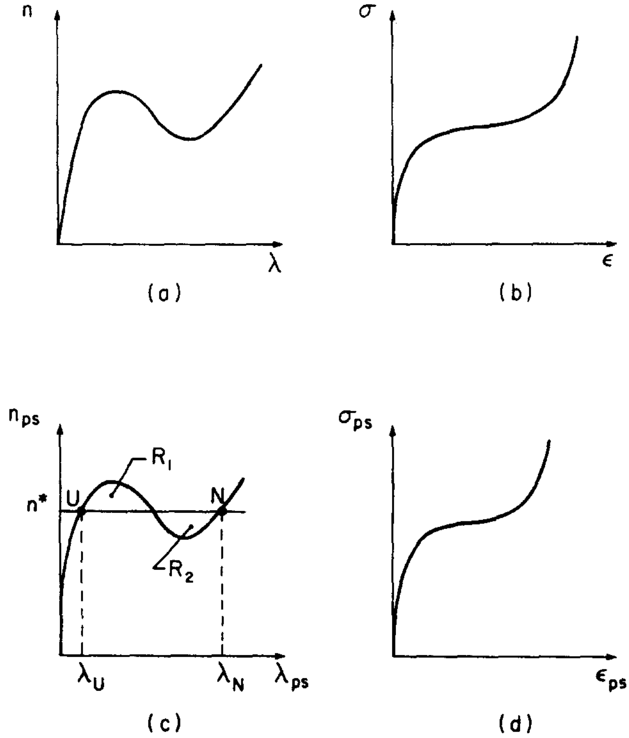

Fig. 2. Stress–strain curves for uniaxial and plane-strain tension. Nominal stress (n, n_{ps}) vs stretch (λ, λ_{ps}) and true stress (σ, σ_{ps}) vs logarithmic strain ($\varepsilon, \varepsilon_{ps}$).

In the analyses mentioned above, isotropic-hardening J_2 flow theory of plasticity was used to characterize the inelastic multiaxial stress–strain behaviour of polymers. Both rate-dependent and rate-independent versions of this theory were employed. Here, we carry out a comprehensive model study of necking and neck propagation in polymeric materials under plane-strain tensile loading. Anisotropic (kinematic) hardening models of plasticity are considered along with isotropic hardening. Approximate one- and two-dimensional analyses, analogous to those presented by Hutchinson and Neale (1983) for round bars, are given for steady-state neck propagation along an infinitely long plane-strain tensile specimen. A finite element analysis simulating the entire load–deformation history of a finite length specimen is also carried out. The effects of material rate dependence and anisotropic hardening are discussed, as well as the accuracy and applicability of the approximate analyses.

2. APPROXIMATE ANALYSES OF STEADY-STATE NECK PROPAGATION

In this section, we present two analyses for steady-state neck propagation along a plane-strain tension specimen. These unidimensional (Maxwell line) and two-dimensional solutions are analogous to those given by Hutchinson and Neale (1983) for a circular cylindrical tensile specimen.

2.1. *Maxwell line analysis*

We consider an infinitely long specimen with uniform properties and a uniform thickness $2h_0$ in the undeformed state. The stress–strain behaviour of the material in *uniaxial tension* is of the form sketched in Fig. 2(a), where the nominal stress (n) reaches a peak, falls to a local minimum, and then increases monotonically with further stretching (λ). The uniaxial true stress (σ)–logarithmic strain (ε) curve is as shown in Fig. 2(b), where the re-stiffening effect observed at high strains produces the upturn in the nominal stress–stretch curve. For uniform *plane-strain tension*, the corresponding curves are as shown in Figs 2(c) and (d).

To simplify the analysis, the material is taken to be incompressible. It is further assumed that the material possesses a strain energy density function W. In *uniaxial* tension, the strain energy density of the material is related to the uniaxial data by

$$W = \int_0^{\lambda} n \, d\lambda = \int_0^{\varepsilon} \sigma \, d\varepsilon. \tag{1}$$

A neck is assumed to have formed at some point along the specimen and then to have spread a distance sufficient to ensure that the transition front between the necked and unnecked regions is advancing under steady-state conditions. The material far ahead of the front is taken to be at rest while the necked section far behind the transition is pulled at velocity V. The transition front moves with velocity C towards the unnecked region (see Fig. 1).

Far ahead of the transition in the unnecked region, the material is in a state of uniform plane-strain tension and we denote the nominal stress and stretch in this state by (n_U, λ_U). Far behind the transition, the necked material is also assumed to be in a state of uniform plane-strain tension given by (n_N, λ_N). The strain energy density difference between states U and N for a particle passing through the transition is the same as if it experienced a purely uniform plane-strain history between these states since a strain energy density W is assumed to exist. That is

$$W_N - W_U = \int_{\lambda_U}^{\lambda_N} n_{ps} \, d\lambda_{ps} \tag{2}$$

which is just the area under the nominal stress–strain curve for plane-strain tension between the stretches $\lambda_{ps} = \lambda_U$ and λ_N.

Continuity, together with incompressibility, implies

$$C = V\left[\frac{\lambda_N}{\lambda_U} - 1\right]^{-1}. \tag{3}$$

If h_U and h_N denote the half-thickness of the specimen far ahead and behind the transition, then

$$\lambda_U h_U = \lambda_N h_N = h_0 \tag{4}$$

and

$$n_{ps} = P/2h_0 \tag{5}$$

where P is the load per unit width carried by the specimen.

In a unit of time, the pulling load does work PV, while the transition front has translated forward a distance C. To evaluate the change in strain energy in the specimen during this unit of time, one needs only note that to an observer moving with the front, the specimen appears unchanged. In effect, a segment of volume $2Ch_U$ from far ahead of the transition has been transferred far behind the transition. The increase in strain energy is $2Ch_U(W_N - W_U)$. The steady-state energy balance is therefore

$$PV = 2Ch_U(W_N - W_U). \tag{6}$$

Dividing by $2h_0$ and using eqns (3)–(5), one can write the energy balance as

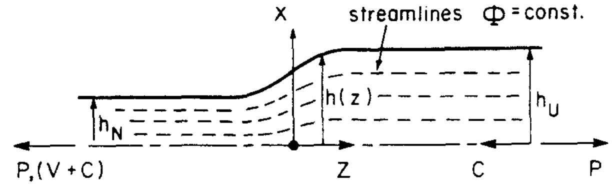

Fig. 3. Conventions for analysis of plane-strain steady-state neck propagation.

$$n_{ps}(\lambda_N - \lambda_U) = W_N - W_U. \tag{7}$$

The graphical solution to eqn (7) is shown in Fig. 2(c). By eqn (2), $W_N - W_U$ is the area under the curve of n_{ps} vs λ_{ps} between λ_U and λ_N, while $n_{ps}(\lambda_N - \lambda_U)$ is the area of the rectangle superimposed on the figure. The equality of these two areas required by eqn (7) is equivalent to the requirement that the areas designated by R_1 and R_2 be equal. In the literature of phase transitions, the horizontal line at $n_{ps} = n^*$ connecting the states U and N is called the Maxwell line.

2.2. *Two-dimensional analysis of steady-state neck propagation*

In the previous analysis, it was possible to determine the states on either side of the transition, independently of the details of the behaviour in the transition, because the strain energy difference $W_N - W_U$ could be determined in terms of the uniform plane-strain tension states U and N. Obviously, this does not hold for an inelastic solid since its stress–strain behaviour is inherently path dependent. Thus, $W_N - W_U$ cannot be calculated from plane-strain tension data alone. For an inelastic solid, it is essential to analyse the full two-dimensional problem to obtain the states on either side of the transition.

The two-dimensional approximate analysis of steady-state neck propagation is carried out for an infinitely long plane-strain specimen made of an incompressible material with a uniaxial true stress–true strain (σ–ε) and nominal stress–stretch (n, λ) curve similar to those depicted in Fig. 2. The multiaxial constitutive relations will be specified in the next section.

A Cartesian coordinate system (x, y, z) is used as a reference (Fig. 3). Without loss of generality, we take this system to be situated in the transition front and to be translating with it along the specimen axis at a constant velocity C. Because of the plane-strain condition, the particle velocities become

$$\mathbf{v} = v_x\mathbf{i} + v_z\mathbf{k} \tag{8}$$

where **i**, **k** are unit base vectors in the x- and z-directions, respectively, and the components v_x, v_z are functions of x and z only. The boundary conditions for the coordinate system translating with the front are

$$\begin{aligned} v_x &= 0, \quad v_z = -C && \text{as} \quad z \to \infty \\ v_x &= 0, \quad v_z = -(V+C) && \text{as} \quad z \to -\infty. \end{aligned} \tag{9}$$

The profile of the specimen during neck propagation is such that the cross-sections become uniform far away from the transition front with a thickness $h(z) = h_U$ as $z \to \infty$ and $h(z) = h_N$ as $z \to -\infty$ and the slopes $h'(z)$ approaching zero as $z \to \pm\infty$. Since $\lambda_N/\lambda_U = h_U/h_N$, the continuity relation (3) becomes

$$V = C\left[\frac{h_U}{h_N} - 1\right]. \tag{10}$$

The Eulerian strain-rate components, associated with the velocity field (8), are as follows:

$$\dot{\varepsilon}_{xx} = v_{x,x}, \quad \dot{\varepsilon}_{yy} = 0, \quad \dot{\varepsilon}_{zz} = v_{z,z}, \quad \dot{\varepsilon}_{xz} = \tfrac{1}{2}(v_{x,z}+v_{z,x}), \quad \dot{\varepsilon}_{yx} = \dot{\varepsilon}_{yz} = 0 \tag{11}$$

where a comma denotes partial differentiation. Incompressibility requires that $\dot{\varepsilon}_{xx}+\dot{\varepsilon}_{zz} = 0$. This suggests that a stream function $\Phi(x,z)$ be introduced such that

$$v_x = \Phi_{,z}, \qquad v_z = -\Phi_{,x} \tag{12}$$

where curves Φ = const. identify the streamlines of the flow. The strain-rate components are then given by

$$\begin{aligned} \dot{\varepsilon}_{xx} &= \Phi_{,xz} \\ \dot{\varepsilon}_{zz} &= -\Phi_{,xz} \\ \dot{\varepsilon}_{xz} &= \tfrac{1}{2}[\Phi_{,zz}-\Phi_{,xx}]. \end{aligned} \tag{13}$$

Numerical solutions for the above problem will be obtained via the principle of virtual velocities. In this case, the principle takes the form

$$\delta I = 2\int_{-\infty}^{\infty}\int_{0}^{h(z)} [s_{ij}\,\delta\dot{\varepsilon}_{ij}]\,\mathrm{d}x\,\mathrm{d}z - P\,\delta V = 0 \tag{14}$$

where the stress deviator s_{ij} is related to the Cauchy stress tensor by $s_{ij} = \sigma_{ij}-\frac{1}{3}\delta_{ij}\sigma_{kk}$, and δ_{ij} is the Kronecker delta. The volume of integration in eqn (14) corresponds to that defined by the steady-state profile $h(z)$. The spatial distribution of s_{ij} depends on the velocity field $\mathbf{v}$ and the constitutive law of the material. This distribution can be obtained by integrating the constitutive equations along the streamlines, as explained in the next section.

In the analysis, we restrict attention to stream functions of the form

$$\Phi(x,z) = Cx\frac{h_{\mathrm{U}}}{h(z)} \tag{15}$$

which represents an approximate solution of the most general separated form $\Phi = F(x)G(z)$ that satisfies boundary conditions (9). For this choice, v_z is independent of x, which implies that a plane of material points perpendicular to the axis of the specimen remains plane as it passes through the neck transition. The velocity field is thus completely specified by the profile thickness $h(z)$ of the specimen.

Substituting eqn (15) into eqns (13) gives

$$\begin{aligned} \dot{\varepsilon}_{xx} &= -\dot{\varepsilon}_{zz} = -\frac{Ch_{\mathrm{U}}}{h^2}h' \\ \dot{\varepsilon}_{xz} &= \frac{Cxh_{\mathrm{U}}}{2h^3}[2(h')^2-hh''] \end{aligned} \tag{16}$$

where a prime denotes differentiation with respect to z.

The approximate solution is obtained by satisfying the variational equation, eqn (14), using the Ritz technique. The following non-dimensional quantities are introduced

$$\bar{h} = \frac{h}{h_{\mathrm{U}}}, \qquad \bar{z} = \frac{z}{h_{\mathrm{U}}}, \qquad \bar{x} = \frac{x}{h_{\mathrm{U}}} \tag{17}$$

and a prime will now designate differentiation with respect to $\bar{z}$. In the Ritz procedure, we describe the profile thickness in terms of a thickness-reduction parameter $\bar{h}_{\mathrm{N}} = h_{\mathrm{N}}/h_{\mathrm{U}}$ and k additional coefficients c_i. We determine the values of $\bar{h}_{\mathrm{N}}$ and the c_i through the variational principle (14). We have $\bar{h} = \bar{h}(\bar{h}_{\mathrm{N}}, c_i)$, $i = 1,\ldots,k$ so that

$$
\begin{aligned}
\delta\bar{h} &= \sum_{i=0}^{k} \frac{\partial \bar{h}}{\partial c_i}\,\delta c_i \equiv \sum_{i=0}^{k} \bar{h}_i\,\delta c_i \\
\delta\bar{h}' &= \sum_{i=0}^{k} \frac{\partial \bar{h}'}{\partial c_i}\,\delta c_i \equiv \sum_{i=0}^{k} \bar{h}'_i\,\delta c_i \\
\delta\bar{h}'' &= \sum_{i=0}^{k} \frac{\partial \bar{h}''}{\partial c_i}\,\delta c_i \equiv \sum_{i=0}^{k} \bar{h}''_i\,\delta c_i.
\end{aligned}
\tag{18}
$$

(Note that $\bar{h}'_i \equiv \partial\bar{h}'/\partial c_i$ is not equal to $(\bar{h}_i)'$ in general, and similarly, $\bar{h}''_i \equiv \partial\bar{h}''/\partial c_i \neq (\bar{h}_i)''$.) Above and in the following, $c_0 \equiv \bar{h}_{\mathrm{N}}$.

From eqns (16)–(18) and the relation $s_{kk} = 0$, we obtain the following for the integrand in eqn (14):

$$
s_{ij}\,\delta\dot{\varepsilon}_{ij} = \frac{C}{h_{\mathrm{U}}}\sum_{i=0}^{k}\left[f_0\bar{h}_i + f_1\bar{h}'_i + f_2\bar{h}''_i\right]\delta c_i + \frac{f_3}{h_{\mathrm{U}}}\,\delta C
\tag{19}
$$

with

$$
\begin{aligned}
f_0 &= -\frac{2}{\bar{h}^3}\left\{2s_{zz}\bar{h}' + s_{xz}\frac{\bar{x}}{\bar{h}}\left[\psi + (\bar{h}')^2\right]\right\} \\
f_1 &= \frac{2}{\bar{h}^2}\left[s_{zz} + 2s_{xz}\frac{\bar{x}}{\bar{h}}(\bar{h}')\right] \\
f_2 &= -\frac{1}{\bar{h}^2}\,s_{xz}\bar{x} \\
f_3 &= \frac{1}{\bar{h}^2}\left[2s_{zz}\bar{h}' + s_{xz}\frac{\bar{x}}{\bar{h}}\psi\right]
\end{aligned}
\tag{20}
$$

and

$$
\psi = 2(\bar{h}')^2 - \bar{h}\bar{h}''.
$$

The continuity relation gives

$$
\delta V = -\frac{C}{\bar{h}_{\mathrm{N}}^2}\,\delta\bar{h}_{\mathrm{N}} + \left(\frac{1}{\bar{h}_{\mathrm{N}}} - 1\right)\delta C.
\tag{21}
$$

By setting the coefficients of $\delta\bar{h}_{\mathrm{N}}$ and δC equal to zero in eqn (14), we obtain the following set of equations:

$$
\begin{aligned}
b_0 &= \frac{P}{2h_{\mathrm{U}}} + \int_{-\infty}^{\infty}\left[g_0\bar{h}_0 + g_1\bar{h}'_0 + g_2\bar{h}''_0\right]\mathrm{d}\bar{z} = 0 \\
b_i &= \int_{-\infty}^{\infty}\left[g_0\bar{h}_i + g_1\bar{h}'_i + g_2\bar{h}''_i\right]\mathrm{d}\bar{z} = 0 \qquad i = 1,2,\ldots,k \\
b_{k+1} &= \frac{P}{2h_{\mathrm{U}}}\bar{h}_{\mathrm{N}}(1 - \bar{h}_{\mathrm{N}}) - \int_{-\infty}^{\infty} g_3\,\mathrm{d}\bar{z} = 0
\end{aligned}
\tag{22}
$$

where

$$g_i = \bar{h}_{\mathrm{N}}^2 \int_0^{\bar{h}(z)} f_i \, \mathrm{d}\bar{x} \qquad i = 0, 1, 2, 3. \tag{23}$$

The last equation of the set of eqns (22) can be written as

$$PV = \int_{\bar{V}} s_{ij}\dot{\varepsilon}_{ij} \, \mathrm{d}\bar{V} \tag{24}$$

where $\bar{V}$ is the volume. This is simply the work balance relation equivalent to eqn (7).

The rate-independent problem is a non-linear eigenvalue problem for the quasi-static conditions assumed. When material rate dependence is present, the load P is a function of the pull velocity V. Then eqns (22) and (10) give a set of $(k+3)$ equations for the $(k+3)$ parameters P, C, $\bar{h}_{\mathrm{N}}$ and c_i $(i = 1, \ldots, k)$.

Numerical results will be given for the following two-parameter description of the thickness profile

$$\bar{h}(z) = \tfrac{1}{2}[(1+\bar{h}_{\mathrm{N}})+(1-\bar{h}_{\mathrm{N}}) \tanh{(\beta\bar{z})}] \tag{25}$$

where $c_1 \equiv \beta$ is a measure of the sharpness of the transition front. This profile satisfies the boundary conditions at $z = \pm\infty$. Substituting eqn (25) into eqn (22) gives three equations of the form of eqn (22) to determine P, $\bar{h}_{\mathrm{N}} = h_{\mathrm{N}}/h_{\mathrm{U}}$ and β.

3. CONSTITUTIVE LAWS

The constitutive laws employed with the previous two-dimensional analysis are finite strain versions of J_2 deformation theory of plasticity as well as isotropic and kinematic hardening versions of J_2 flow theory of plasticity. The flow theory solid will serve as a model material to characterize the inelastic features of neck propagation even though it is perhaps not entirely adequate for describing the real multiaxial behaviour of polymers at large strains.

3.1. *J_2 flow theory*

3.1.1. *Isotropic hardening.* We first consider incompressible, time-independent material behaviour. The constitutive law takes the following form:

$$\overset{*}{s}_{ij} = \frac{2E}{3}\left(\dot{\varepsilon}_{ij} - \frac{1}{q}s_{kl}\dot{\varepsilon}_{kl}s_{ij}\right) \tag{26}$$

where

$$q = \frac{3}{2}\frac{H}{E} + \frac{2}{3}\sigma_{\mathrm{e}}^2 \tag{27}$$

and

$$H = \left(\frac{3}{2\sigma_{\mathrm{e}}}\right)^2\left[\frac{1}{E_{\mathrm{t}}} - \frac{1}{E}\right]. \tag{28}$$

In these expressions $\overset{*}{s}_{ij}$ denotes the Jaumann rate of the stress deviator, E is the elastic modulus and $\sigma_{\mathrm{e}} = (3s_{ij}s_{ij}/2)^{1/2}$ represents the effective stress. The tangent modulus E_{t} corresponds to the slope of the uniaxial true stress–logarithmic strain curve at the current stress level σ_{e}.

The effective strain rate is defined as

$$\dot{\varepsilon}_e = (\tfrac{2}{3}\dot{\varepsilon}_{ij}\dot{\varepsilon}_{ij})^{1/2}. \tag{29}$$

In simple uniaxial tension, the effective stress and effective strain are equal to the true stress σ and logarithmic strain ε, respectively. The σ_e–ε_e curve for uniaxial tension is assumed to hold for multiaxial stress histories. A true stress–natural strain curve with features illustrated in Figs 2(b) and (d) are employed in this analysis.

For the steady-flow problem formulated in the previous section, the fields $\dot{\varepsilon}_{ij}$ are specified by the wave speed C and profile thickness of the specimen $h(z)$. To determine the spatial distribution of s_{ij}, we note first that from the plane-strain condition $\varepsilon_{yy} = 0$, so that at $z = \infty$ we have $s_{yy} = 0$, $s_{xx}^{\mathrm{U}} = -\sigma_{zz}^{\mathrm{U}}/2$, $s_{zz}^{\mathrm{U}} = -s_{xx}^{U}$, and all other $s_{ij}^{U} = 0$. To obtain the stress deviator components, we integrate along the streamlines $\Phi = \text{const.}$ as follows:

$$s_{ij} = s_{ij}^{\mathrm{U}} + \int_{\infty}^{(x,z)} \frac{\dot{s}_{ij}}{|\mathbf{v}|}\,\mathrm{d}l \tag{30}$$

where $\mathrm{d}l = |\mathbf{v}|\,\mathrm{d}z/v_z = |\mathbf{v}|\,\mathrm{d}x/v_x$ represents an element of arc length along the streamline and $\dot{s}_{ij}$ denotes the material rate of s_{ij} as obtained from eqn (26) and the relation between material and Jaumann rates of change.

For rigid–plastic behaviour, the constitutive law becomes

$$s_{ij} = \frac{2}{3}\frac{\sigma_e}{\dot{\varepsilon}_e}\dot{\varepsilon}_{ij}. \tag{31}$$

In this case, the s_{ij} distribution is computed by integrating the increments $\dot{\varepsilon}_e$ along the streamlines. The integration procedure outlined above gives

$$\varepsilon_e = \frac{2}{\sqrt{3}}\varepsilon_{zz}^{\mathrm{U}} - \frac{2}{\sqrt{3}}\int_{\infty}^{\bar{z}} \frac{1}{\bar{h}}\left\{(\bar{h}')^2 + \frac{1}{4}\left(\frac{\bar{x}}{\bar{h}}\right)^2 [2(\bar{h}')^2 - \bar{h}\bar{h}'']^2\right\}^{1/2} \mathrm{d}\bar{z}. \tag{32}$$

Here $\bar{x} = \bar{x}(z)$ is the coordinate in the thickness direction along the particular streamline considered and the first term on the right-hand side of eqn (32) is the value of ε_e at $z = \infty$. Having computed the ε_e distribution, we can calculate the value of the effective stress σ_e at each point using the uniaxial true stress–natural strain curve.

Rate-dependent material behaviour is incorporated in the rigid–plastic model as follows. The general form of $\sigma_e = \sigma_s(\varepsilon_e)$ for the quasi-static rate-independent relation (subscript s denotes static) is replaced by a relation of the form

$$\sigma_e = \sigma_s(\varepsilon_e)\left[1 + m\ln\left(1 + \frac{\dot{\varepsilon}_e}{\dot{\varepsilon}_{\mathrm{R}}}\right)\right] \tag{33}$$

where m is a strain-rate hardening index and $\dot{\varepsilon}_{\mathrm{R}}$ is a reference strain rate. The above curve, eqn (33), reduces to the rate-independent relation when $m = 0$ and in the quasi-static limit ($\dot{\varepsilon}_e \rightarrow 0$). A relation of the form of eqn (33) accounts for the effect of material strain-rate dependence in a simple way, and it cannot be expected to accurately represent material behaviour for arbitrary histories of stress, strain, and strain rate. This model should be sufficient, however, for giving a qualitative indication of the effects of material rate sensitivity on neck propagation.

3.1.2. *Kinematic hardening.* With this model, the initial yield surface has the form $F(\sigma) = \text{const.}$, and is assumed to translate rigidly in stress space during plastic deformation. The current yield surface is given by

$$\tfrac{3}{2}(s_{ij}-\alpha_{ij})(s_{ij}-\alpha_{ij}) = \sigma_Y^2 \tag{34}$$

where α_{ij} is the deviator specifying the current position of the yield-surface origin and σ_Y is the initial yield stress.

The condition $\dot{\sigma}_Y = 0$ with Ziegler's rule gives

$$\overset{*}{\alpha}_{ij} = \frac{3}{2\sigma_Y^2}\tilde{s}_{ij}\tilde{s}_{kl}\overset{*}{\sigma}_{kl} \tag{35}$$

where $\tilde{s}_{ij} = s_{ij}-\alpha_{ij}$. The plastic flow law becomes

$$\dot{\varepsilon}_{ij} = \left(\frac{3}{2\sigma_Y}\right)^2\frac{1}{E_t}\tilde{s}_{ij}\tilde{s}_{kl}\overset{*}{\sigma}_{kl}. \tag{36}$$

Inverting this gives

$$\tilde{s}_{ij} = \frac{2}{3}\frac{\sigma_Y}{\dot{\varepsilon}_c}\dot{\varepsilon}_{ij} \tag{37}$$

where

$$\dot{\varepsilon}_c \equiv (\tfrac{2}{3}\dot{\varepsilon}_{ij}\dot{\varepsilon}_{ij})^{1/2}. \tag{38}$$

Note that $\dot{\varepsilon}_c$ as defined here is not necessarily the same as the effective strain rate $\dot{\varepsilon}_e$ arising from the plastic work postulate $s_{ij}\dot{\varepsilon}_{ij} = \sigma_e\dot{\varepsilon}_e$. In eqn (36), E_t is the tangent modulus at the current effective stress level σ_e. In view of eqn (36), eqn (35) can be conveniently expressed as

$$\overset{*}{\alpha}_{ij} = \tfrac{2}{3}E_t\dot{\varepsilon}_{ij}. \tag{39}$$

In this study, the following three methods for evaluating the current effective stress level σ_e were considered:

(i) the relation

$$\sigma_e = \sigma_Y + (\tfrac{3}{2}\alpha_{ij}\alpha_{ij})^{1/2} \tag{40}$$

as proposed by Tvergaard (1978);

(ii) an incremental relation based on the equivalent plastic-work postulate, as suggested by Mear and Hutchinson (1985)

$$\dot{\sigma}_e = \frac{E_t}{\sigma_e}s_{ij}\dot{\varepsilon}_{ij}; \tag{41}$$

(iii) a model used by Nagtegaal and de Jong (1982), where eqn (38) is taken as the effective strain rate. Integrating this gives ε_e and the uniaxial σ_e–ε_e relation is used to determine σ_e and the tangent modulus E_t.

Using eqn (39) and the expression relating Jaumann rates and material rates of change, we integrate along the streamlines to obtain α_{ij}. This gives

$$\alpha_{zz} = \alpha_{zz}^{\mathrm{U}} - \int_{\infty}^{\bar{z}} \frac{1}{\bar{h}} \left\{ \frac{2}{3} E_{\mathrm{t}} \bar{h}' - \alpha_{xz} \frac{\bar{x}}{\bar{h}} [2(\bar{h}')^2 - \bar{h}\bar{h}''] \right\} \mathrm{d}\bar{z} \tag{42}$$

$$\alpha_{xz} = \alpha_{xz}^{\mathrm{U}} - \int_{\infty}^{\bar{z}} \frac{\bar{x}}{\bar{h}^2} [2(\bar{h}')^2 - \bar{h}\bar{h}''] (\tfrac{1}{3} E_{\mathrm{t}} + \alpha_{zz}) \, \mathrm{d}\bar{z}. \tag{43}$$

For the plane-strain case studied here, we have $\alpha_{zz}^{\mathrm{U}} = \sigma_{zz}/2 - \sigma_{\mathrm{Y}}/\sqrt{3}$, $\alpha_{xx}^{\mathrm{U}} = -\alpha_{zz}^{\mathrm{U}}$, $\alpha_{yy}^{\mathrm{U}} = 0$, $\alpha_{xz}^{\mathrm{U}} = 0$. Once the α_{ij} are computed, we calculate the spatial distribution of s_{ij} at each point using eqn (37) and the relation $s_{ij} = \tilde{s}_{ij} + \alpha_{ij}$.

Rate-dependent material behaviour is incorporated using eqn (33) as in the isotropic hardening case. Such a dependence implies that $\dot{\sigma}_{\mathrm{Y}} \neq 0$ and that the yield surface origin translates according to

$$\overset{*}{\alpha}_{ij} = \tfrac{2}{3} E_{\mathrm{t}} \dot{\varepsilon}_{ij} - \tfrac{2}{3} \sigma_{\mathrm{Y}} \frac{m \ddot{\varepsilon}_{\mathrm{e}}}{(\dot{\varepsilon}_{\mathrm{R}} + \dot{\varepsilon}_{\mathrm{e}})} \frac{\dot{\varepsilon}_{ij}}{\dot{\varepsilon}_{\mathrm{e}}} \tag{44}$$

where

$$\ddot{\varepsilon}_{\mathrm{e}} = \dot{\varepsilon}_{\mathrm{e},k} v_k. \tag{45}$$

To simplify the analysis, we shall only employ the Nagtegaal–de Jong model to study rate effects since this is the only model for which $\dot{\varepsilon}_{\mathrm{e}}$ can be expressed explicitly in terms of the velocity field (12). In this case, the terms $\tilde{s}_{ij}$ are given by

$$\tilde{s}_{ij} = \tfrac{2}{3} \sigma_{\mathrm{Y}} \left[1 + m \ln \left(1 + \frac{\dot{\varepsilon}_{\mathrm{e}}}{\dot{\varepsilon}_{\mathrm{R}}} \right) \right] \frac{\dot{\varepsilon}_{ij}}{\dot{\varepsilon}_{\mathrm{e}}}. \tag{46}$$

3.2. J_2 *deformation theory*

The finite strain J_2 deformation theory constitutive law considered is a non-linear elastic law for isotropic incompressible solids. Aspects of this law were discussed in previous papers (e.g. Hutchinson and Neale (1978, 1981)). In applying it here, we make use of Hill's "principal-axes techniques" (Hill, 1970) for finitely deformed isotropic elastic solids.

Let s_i and $\varepsilon_i = \ln \lambda_i$ denote the principal components of the Cauchy stress deviator and principal logarithmic strains, respectively (λ_i are the principal stretches). The logarithmic strain tensor $\boldsymbol{\varepsilon}$ is by definition, coaxial with the Lagrangian strain ellipsoid. The strain rates $\dot{\varepsilon}_1$, etc. are identically equal to the Eulerian strain-rate components $\dot{\varepsilon}_{11}$, etc. referred to the current axes (x'_1, x'_2) of the Eulerian strain ellipsoid. Transforming the strain-rate components from the (x, z) reference system to the principal Eulerian axes (x'_1, x'_2) gives

$$\begin{aligned} \dot{\varepsilon}_1 &= \dot{\varepsilon}'_{11} = \tfrac{1}{2}[(\dot{\varepsilon}_{zz} + \dot{\varepsilon}_{xx}) + (\dot{\varepsilon}_{zz} - \dot{\varepsilon}_{xx}) \cos 2\phi] + \dot{\varepsilon}_{xz} \sin 2\phi \\ \dot{\varepsilon}_2 &= \dot{\varepsilon}'_{22} = \tfrac{1}{2}[(\dot{\varepsilon}_{zz} + \dot{\varepsilon}_{xx}) - (\dot{\varepsilon}_{zz} - \dot{\varepsilon}_{xx}) \cos 2\phi] - \dot{\varepsilon}_{xz} \sin 2\phi \\ \dot{\varepsilon}'_{12} &= -\tfrac{1}{2}(\dot{\varepsilon}_{zz} - \dot{\varepsilon}_{xx}) \sin 2\phi + \dot{\varepsilon}_{xz} \cos 2\phi \end{aligned} \tag{47}$$

where ϕ represents the orientation of the x'_1-axis with respect to the z-axis.

Hill (1970) gives the following for the rate of rotation of the principal Eulerian axes:

$$\dot{\phi} = \frac{\lambda_1^2 + \lambda_2^2}{\lambda_1^2 - \lambda_2^2} \dot{\varepsilon}'_{12} + \dot{\Omega} \tag{48}$$

where $\dot{\Omega} = (v_{x,z} - v_{z,x})/2$ represents the spin of a material element in the x–z plane. By integrating along streamlines as described earlier, we get

$$\begin{aligned}\phi &= \phi^{\mathrm{U}} - \int_{\infty}^{z} \frac{h}{h_{\mathrm{U}}} \frac{\dot{\phi}}{C}\,\mathrm{d}z \\ \varepsilon_i &= \varepsilon_i^{\mathrm{U}} - \int_{\infty}^{z} \frac{h}{h_{\mathrm{U}}} \frac{\dot{\varepsilon}_i}{C}\,\mathrm{d}z\end{aligned} \tag{49}$$

where $\phi^{\mathrm{U}} = 0$, $\varepsilon_1^{\mathrm{U}} = \varepsilon_{\mathrm{U}}$, $\varepsilon_2^{\mathrm{U}} = -\varepsilon_{\mathrm{U}}$ designate the values at $z = \infty$.

To determine the current stress deviator components, we make use of the fact that, for an isotropic elastic solid, the principal directions of the Cauchy deviatoric stress tensor s must coincide with the principal Eulerian axes x_i'. The finite strain J_2 deformation theory law is expressed in terms of the principal components of s and $\boldsymbol{\varepsilon}$ and has the form (Hutchinson and Neale, 1978)

$$s_i = \frac{2}{3} \frac{\sigma_e}{\varepsilon_e} \varepsilon_i \tag{50}$$

where the effective strain ε_e is defined as follows:

$$\varepsilon_e = (\tfrac{2}{3}\varepsilon_i \varepsilon_i)^{1/2}. \tag{51}$$

The effective stress and strain are related by the uniaxial relation $\sigma_e = \sigma_s(\varepsilon_e)$. Thus, for a given flow field prescribed by the wave speed C and thickness profile $h(z)$, we can integrate eqn (49) along the streamlines $\Phi =$ const. to determine the orientations of the principal axes ϕ and total principal strains ε_i. Equations (50) and (51), together with the uniaxial stress–strain relation give the principal stress deviators s_i. Transforming back to the (x, z) reference system gives

$$\begin{aligned} s_{xx} &= \tfrac{1}{2}[(s_1 + s_2) - (s_1 - s_2)\cos 2\phi] \\ s_{zz} &= \tfrac{1}{2}[(s_1 + s_2) + (s_1 - s_2)\cos 2\phi] \\ s_{xz} &= \tfrac{1}{2}(s_1 - s_2)\sin 2\phi. \end{aligned} \tag{52}$$

4. RESULTS OF THE APPROXIMATE ANALYSES

In this section we present results showing some characteristic features of plane-strain neck propagation, as well as comparisons between the predictions of the various models of material behaviour. The numerical procedure associated with the two-dimensional analysis is identical to that devised by Hutchinson and Neale (1983).

The particular form of the *uniaxial* stress–strain curve adopted is as follows:

$$\sigma = \begin{cases} E\varepsilon & \text{if} \quad \varepsilon \leqslant \varepsilon_y \\ \alpha k \varepsilon^{\mathrm{N}} & \text{if} \quad \varepsilon_y \leqslant \varepsilon \leqslant \varepsilon_0 \,. \\ k \exp(M\varepsilon^2) & \text{if} \quad \varepsilon \geqslant \varepsilon_0 \end{cases} \tag{53}$$

We consider k, ε_0, M, ε_y as the independent material constants and impose continuity of the stress σ at $\varepsilon = \varepsilon_y$ and $\varepsilon = \varepsilon_0$, as well as continuity of the tangent modulus $\mathrm{d}\sigma/\mathrm{d}\varepsilon$ at $\varepsilon = \varepsilon_0$. This gives $N = 2M(\varepsilon_0^2)$, $\alpha = \exp(N/2)/\varepsilon_0^{\mathrm{N}}$ and $E/k = \alpha\varepsilon_y^{N-1}$. The rigid–plastic results are obtained using eqns (53) putting $\varepsilon_y = 0$. The above relation describes a monotonically increasing true stress–natural strain curve that excludes the possible occurrence of purely material (shear band) instabilities. Numerical results will be given for the two cases treated previously by Hutchinson and Neale (1983): (i) $M = 0.50$, $\varepsilon_0 = 0.50$, and (ii) $M = 0.25$, $\varepsilon_0 = 1.00$. The value $\varepsilon_y = 0.04$ is employed for the elastic–plastic analyses. The uniaxial curves associated with these choices are such that $n_{\max}/k = P_{\max}/2kh_0 = 0.8883$ and 0.6833, respectively, in plane-strain tension.

Table 1. Comparison of one- and two-dimensional solutions for non-linear elastic solid

Case	M	ε_0	$\varepsilon_{\rm I}^{\rm U}/N$	$h_{\rm N}/h_{\rm U}$	β	$P/P_{\rm max}$	
(i)	0.5	0.5	0.4161	0.3906	—	0.9296	Exact
			0.4146	0.4115	0.9105	0.9289	Numerical
(ii)	0.25	1.00	0.3997	0.1515	—	0.8540	Exact
			0.3964	0.1752	1.5474	0.8514	Numerical

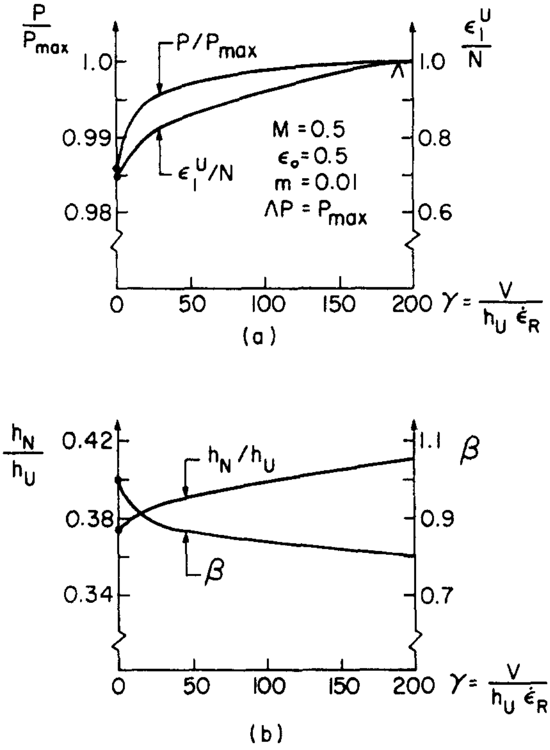

Fig. 4. Results for quasi-static neck propagation in a rate-dependent inelastic solid (isotropic hardening).

First, we compare results for the rate-independent non-linear elastic solid as obtained exactly from the Maxwell line analysis and numerically from the approximate two-dimensional deformation theory analysis. These are summarized in Table 1. The close agreement observed here suggests that a reasonable accuracy can be anticipated for the inelastic two-dimensional analyses. (Note that $\varepsilon_{\rm I}^{\rm U} \equiv \varepsilon_{zz}^{\rm U}$.)

The rigid–plastic isotropic hardening J_2 flow theory results for case (i) of Table 1 are $\varepsilon_{\rm I}^{\rm U}/N = 0.6999$, $h_{\rm N}/h_{\rm U} = 0.3734$, $\beta = 1.0032$, $P/P_{\rm max} = 0.9862$, while for case (ii), we get $\varepsilon_{\rm I}^{\rm U}/N = 0.9816$, $h_{\rm N}/h_{\rm U} = 0.2002$, $\beta = 1.6983$, $P/P_{\rm max} = 0.9999$.

Next, we present results for rate effects with rigid–plastic isotropic hardening J_2 flow theory. In the rate-dependent relation (32), we took $m = 0.01$ and 0.05. The non-dimensional velocity parameter becomes $\gamma = V/(h_{\rm U}\dot{\varepsilon}_{\rm R})$. In Figs 4–7, the pull load, the pull strain, the thickness-reduction ratio and transition front parameter β are given as functions of γ. In these figures, $P_{\rm max}$ is the peak load $(n_{\rm max}2h_0)$ associated with $m = 0$, or equivalently, associated with $\dot{\varepsilon}_{\rm e}/\dot{\varepsilon}_{\rm R} \to 0$ for plane-strain tension. This state is designated by the symbol $\wedge$ on these curves. From Figs 4–7, it can be seen that an increased pull velocity is associated with a higher pull load yet a smoother transition profile (smaller β). A comparison with the previous results of Hutchinson and Neale (1983) for the round bar shows that the condition $P/P_{\rm max} = 1$ is reached at considerably lower pull velocities for the plane-strain specimen than for the corresponding axisymmetric bar.

Results obtained with the elastic–plastic model, assuming isotropic-hardening and rate-independent material behaviour are given in Tables 2(a) and (b) for materials (i) and

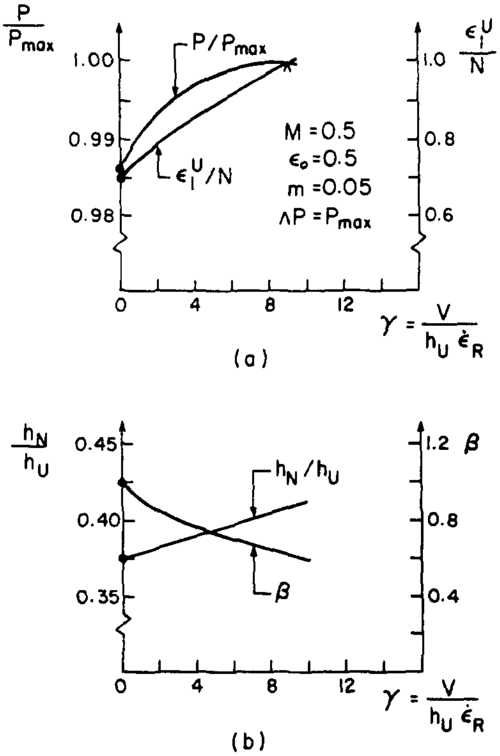

Fig. 5. Results for quasi-static neck propagation in a rate-dependent inelastic solid (isotropic hardening).

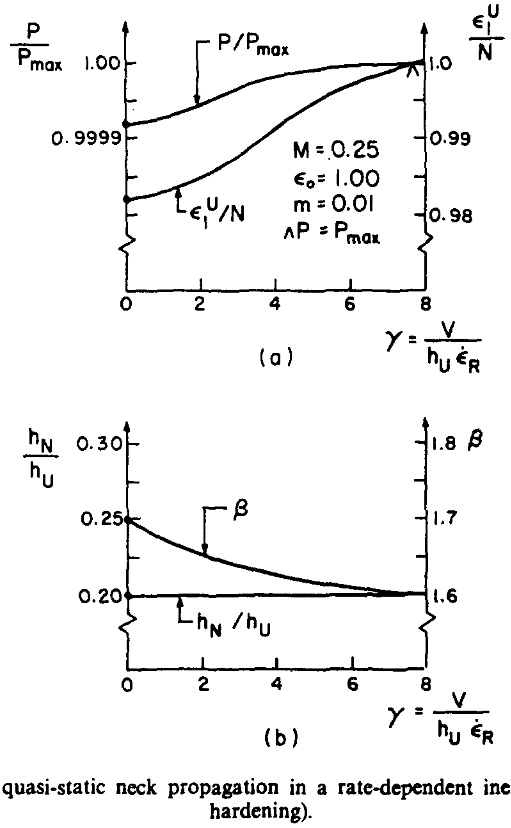

Fig. 6. Results for quasi-static neck propagation in a rate-dependent inelastic solid (isotropic hardening).

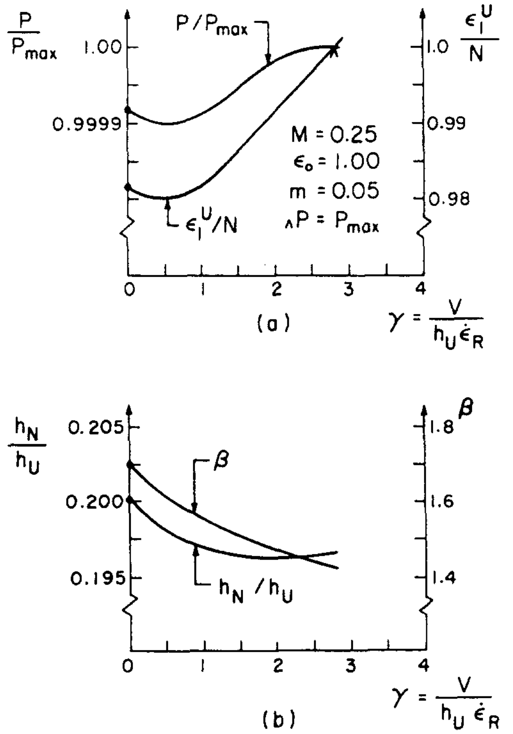

Fig. 7. Results for quasi-static neck propagation in a rate-dependent inelastic solid (isotropic hardening).

Table 2(a). Elastic–plastic results for material (i)

	$M = 0.5$			$\varepsilon_0 = 0.5$		
ε_y	E/k	ε_I^U/N	h_N/h_U	β	P/P_{max}	Case
0.04	15.066	0.5510	0.3709	0.8564	0.9639	Elastic–plastic
0.001	239.63	0.6910	0.3710	0.9938	0.9849	
0.0005	403.11	0.6912	0.3723	0.9950	0.9850	
0	∞	0.6999	0.3734	1.0032	0.9862	Rigid–plastic

Table 2(b). Elastic–plastic results for material (ii)

	$M = 0.25$			$\varepsilon_0 = 1.00$		
ε_y	E/k	ε_I^U/N	h_N/h_U	β	P/P_{max}	Case
0.04	6.62	0.5628	0.1646	1.5195	0.9335	Elastic–plastic
0.001	40.60	0.8472	0.1859	1.6662	0.9935	
0.00001	406.04	0.9687	0.1982	1.6965	0.9998	
0	∞	0.9816	0.2002	1.6983	0.9999	Rigid–plastic

(ii), respectively. The rigid–plastic results are also reproduced in these tables to show how the elastic–plastic results approach the rigid–plastic results as E/k increases (ε_y decreases). From Tables 2(a) and (b), it is obvious that elasticity plays an important role for the range of ε_y values that are typical for polymers. In general, elasticity decreases the pull load and results in a smoother transition profile (smaller β). We also observe here that the elastic–plastic results with $E/k \simeq 400$ closely approximate the corresponding rigid–plastic solutions.

Table 3 shows the kinematic-hardening results for material (i) obtained from the different models discussed in the previous sections. In the same table, we also show the rigid–plastic isotropic hardening results for purposes of comparison. In general, all kinematic-hardening models produce essentially similar results and predict neck propagation at loads somewhat lower than that obtained with isotropic hardening.

Table 3. Rigid–plastic kinematic hardening results for material (i)

$M = 0.5$		$\varepsilon_0 = 0.5$		
ε_l^U/N	h_N/h_U	β	P/P_{max}	Model
0.4414	0.3478	1.2567	0.9375	Tvergaard (1978)
0.4526	0.3592	1.2233	0.9396	Mear–Hutchinson (1985)
0.4670	0.3795	1.1662	0.9447	Nagtegaal–de Jong (1982)
0.6999	0.3734	1.0032	0.9862	Isotropic hardening

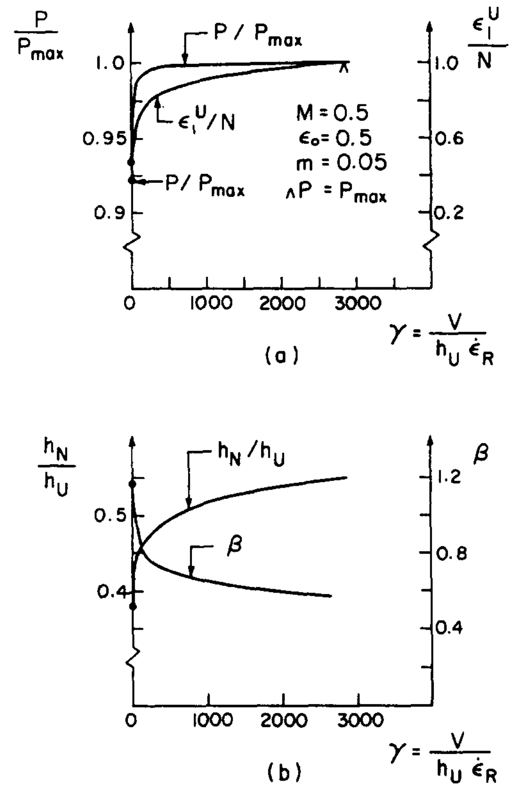

Fig. 8. Results for quasi-static neck propagation in a rate-dependent inelastic solid (kinematic hardening).

The combined effects of kinematic hardening (the Nagtegaal–de Jong model) and material rate dependency ($m = 0.05$) are given in Figs 8 and 9 for materials (i) and (ii), respectively. A comparison with the isotropic hardening counterparts (Figs 5 and 7) shows that significantly larger pull velocities are required with the kinematic-hardening model.

5. FINITE ELEMENT ANALYSIS OF NECKING AND NECK PROPAGATION

A Lagrangian formulation for finitely deformed elastic–plastic solids is employed in the finite element analysis in contrast to the Eulerian description adopted for the approximate analyses of the previous sections. The initial undeformed configuration of the body, with volume $\bar{V}_0$ and surface S, is used as a reference. Material points are identified by convected coordinates x_i in this reference state. The governing equations are written in rate form and solved incrementally.

We restrict this analysis to time-independent elastic–plastic behaviour. The constitutive law is thus of the form

$$\overset{*}{\tau}^{ij} = L^{ijkl}\dot{\eta}_{kl} \tag{54}$$

where L^{ijkl} denotes the tensor of instantaneous moduli, $\overset{*}{\tau}^{ij}$ are the Jaumann rates of the

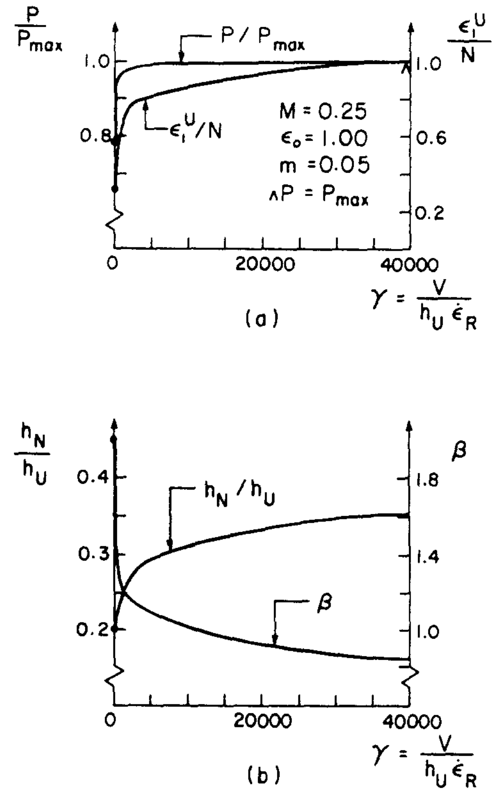

Fig. 9. Results for quasi-static neck propagation in a rate-dependent inelastic solid (kinematic hardening).

Kirchhoff stress tensor τ and $\dot\eta_{ij}$ are the Lagrangian strain-rate components. The contravariant components τ^{ij} are defined with respect to deformed base vectors $\mathbf{G}_i$ and are related to the Cauchy stress components σ^{ij} by $\tau^{ij} = \rho_0\sigma^{ij}/\rho$ where ρ_0 and ρ are the densities in the initial and current states, respectively. Note that whereas the incompressibility condition was required for the streamline approach of the approximate analyses, a small amount of elastic compressibility is retained here for the finite element computations.

The finite element equations are developed using an extremum principle due to Hill (1958, 1959). This principle states that the incremental equilibrium behaviour of the solid is governed by the following variational equation

$$\delta J = 0 \tag{55}$$

with

$$J(\dot u) = \int_{V_0} [(\tfrac{1}{2}L^{ijkl} - G^{il}\tau^{kj})\dot\eta_{ij}\dot\eta_{kl} + \tfrac{1}{2}\tau^{ij}\dot u^k_{,i}\dot u_{k,j}]\,\mathrm{d}\bar V_0 - \int_{S_F} \dot F^i \dot u_i\,\mathrm{d}S. \tag{56}$$

Here G^{ij} is the deformed metric and $\dot u_{i,j}$ are the velocity gradients referred to the undeformed metric. The admissible velocity fields are assumed to satisfy the prescribed kinematic boundary conditions. In eqn (56), S_F represents the part of the surface on which the nominal traction increments $\dot{\mathbf{F}}$ are prescribed.

Finite strain versions of the classical isotropic-hardening and kinematic-hardening J_2 flow theory of plasticity (Hutchinson, 1975; Tvergaard, 1978) are employed. The moduli L^{ijkl} in eqn (54) have the general form

$$L^{ijkl} = \frac{E}{1+\nu}\left[\frac{1}{2}(G^{ik}G^{jl}+G^{jk}G^{il}) + \frac{\nu}{1-2\nu}G^{ij}G^{kl} - \frac{\Lambda}{\bar{q}}\bar{s}^{ij}\bar{s}^{kl}\right] \tag{57}$$

where ν is Poisson's ratio. The parameter $\bar{q}$ is given by

$$\bar{q} = (1+\nu)\frac{\bar{H}}{E} + \frac{2}{3}\bar{\tau}_e^2 \tag{58}$$

and

$$\Lambda = \begin{cases} 1 & \text{if} \quad \bar{s}^{ij}\dot{\eta}_{ij} > 0 \quad \text{and} \quad \bar{\tau}_e = \tau_{cr} \\ 0 & \text{if} \quad \bar{s}^{ij}\dot{\eta}_{ij} \leqslant 0 \quad \text{or} \quad \bar{\tau}_e < \tau_{cr} \end{cases}. \tag{59}$$

The work-hardening parameter $\bar{H}$ is defined below for each of the constitutive models considered.

With isotropic-hardening J_2 flow theory $\bar{s}_{ij}$ is the deviator of the Kirchhoff stress tensor τ_{ij}, given by

$$\bar{s}^{ij} = \tau^{ij} - \tfrac{1}{3}G^{ij}G_{kl}\tau^{kl}. \tag{60}$$

Its invariant J_2 and the corresponding effective Kirchhoff stress $\bar{\tau}_e$ are defined as follows:

$$J_2 = \tfrac{1}{3}\bar{\tau}_e^2 = \tfrac{1}{2}G_{ik}G_{jl}\bar{s}^{ij}\bar{s}^{kl}. \tag{61}$$

For this model τ_{cr} in eqns (59) is given by $\tau_{cr} = (\bar{\tau}_e)_{max}$. By specializing the relations to uniaxial tension, we have

$$\bar{\tau}_e = (\rho_0/\rho)\sigma$$

and

$$\frac{1}{\bar{H}} = \left(\frac{3}{2\bar{\tau}_e}\right)^2\left\{\frac{\rho}{\rho_0}\left[1-(1-2\nu)\frac{\bar{\tau}_e}{E}\right]\frac{1}{E_t} - \frac{1}{E}\right\}. \tag{62}$$

Here the tangent modulus E_t is the slope of the uniaxial true stress–natural strain curve.

With kinematic-hardening J_2 flow theory, the quantity $\bar{s}_{ij}$ is now the deviator

$$\bar{s}^{ij} = \bar{\tau}^{ij} - \tfrac{1}{3}G^{ij}G_{kl}\bar{\tau}^{kl} \tag{63}$$

where

$$\bar{\tau}^{ij} = \tau^{ij} - \xi^{ij} \tag{64}$$

and ξ^{ij} represents the translation of the yield surface centre in the stress space τ^{ij}. $\bar{\tau}_e$ is given by eqn (61) and in eqns (59) $\tau_{cr} = \tau_Y$, the value of the physical component of the Kirchhoff stress at yield. Furthermore, we have

$$\frac{1}{\bar{H}} = \left(\frac{3}{2\tau_Y}\right)^2\left[\frac{1}{E_t} - \frac{1}{E}\right] \tag{65}$$

where contrary to the isotropic-hardening case, the tangent modulus now is the slope of the uniaxial Kirchhoff stress–logarithmic strain curve at the current level τ_e, where τ_e is obtained from an expression analogous to eqn (40), i.e. Tvergaard's (1978) kinematic-hardening model. The difference between σ_e and τ_e however is expected to be small as volume changes arise only from the elastic components.

The yield surface translation is obtained from the expression

$$\overset{*}{\xi}{}^{ij} = (\tau^{ij} - \xi^{ij})\dot{\mu}, \qquad \dot{\mu} > 0 \tag{66}$$

in which

$$\dot{\mu} = \frac{3}{2\tau_Y^2}\bar{s}_{ij}\overset{*}{\tau}{}^{ij}. \tag{67}$$

In the finite element formulation, a rectangular specimen of thickness $2h_0$ and length $2L_0$ in the initial state is considered. A Cartesian coordinate system with $x^1 = x$, $x^2 = y$, $x^3 = z$ is used as a reference. Symmetry with respect to the mid-planes $x = 0$, $z = 0$ is assumed. The displacement components are

$$u_x = u^x = u_x(x,z), \qquad u_y = u^y = 0, \qquad u_z = u^z = u_z(x,z). \tag{68}$$

From the assumed symmetry about $z = 0$ we have

$$\dot{F}^1(x,0) = 0, \qquad \dot{u}_z(x,0) = 0. \tag{69}$$

We consider a specimen with shear-free ends so that the boundary conditions at $z = L_0$ become

$$\dot{F}^1(x,L_0) = 0, \qquad \dot{u}_z(x,L_0) = \dot{U} \tag{70}$$

where $\dot{U}$ is the prescribed increment of axial elongation. The lateral surface ($x = h_0$) of the specimen is taken to be stress free.

In the numerical analysis, an initial geometric nonuniformity is specified to initiate necking. This is done by reducing the thickness of the centre part of the specimen by an amount $\Delta h/h_0$ along a distance L' of its length. In our finite element scheme, quadrilateral elements, each consisting of four triangular linear-displacement elements, are employed. Since the plane-strain case results in constant strain triangles, a central one-point integration scheme is employed to compute the integrals. The resultant load at each increment is obtained by integrating the physical component σ_{zz} over the current cross-section at the end of the specimen. A similar calculation at the mid-plane $z = 0$ is also carried out to verify overall equilibrium. Throughout the computations, the differences in these resultants were kept to within a fraction of 1%.

6. RESULTS OF THE FINITE ELEMENT ANALYSIS

Numerical results have been obtained for a specimen which initially has a length-to-thickness ratio $L_0/h_0 = 4$ and a geometric imperfection in the form of a reduced thickness in the central part of the specimen of $\Delta h = 0.005h_0$. A uniaxial stress–strain curve of the form of eqns (53) with constants $M = 0.5$, $\varepsilon_0 = 0.5$, $\varepsilon_y = 0.04$, $\nu = 0.4$ is assumed. The

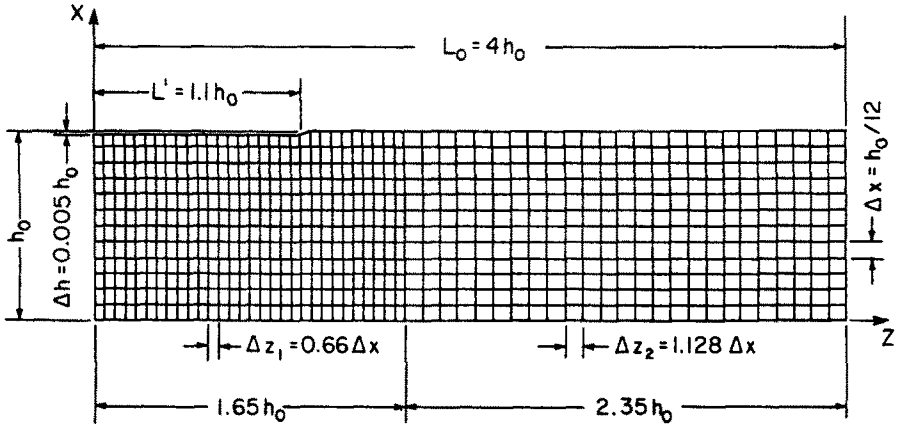

Fig. 10. Finite element mesh (12 × 55) and specimen geometry for the kinematic-hardening study.

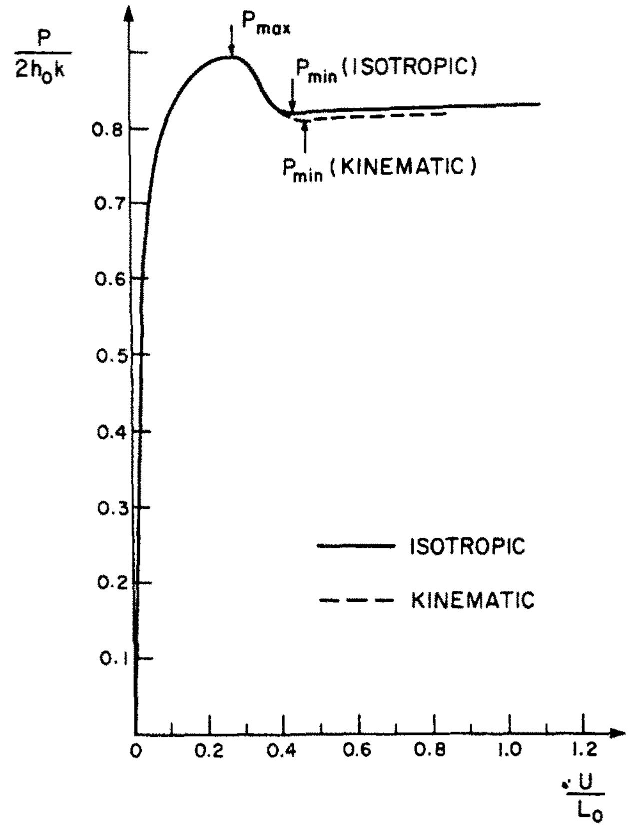

Fig. 11. Computed load–elongation curves.

finite element mesh employed for the kinematic-hardening model is shown in Fig. 10. The same mesh, except with eight equal divisions in the x-direction, was used for the isotropic-hardening simulation. For the isotropic-hardening study, a very small increment size was initially taken in the region $U/L_0 \sim \varepsilon_y$, otherwise an increment size of $\dot{U}/L_0 = 0.001$ was used. Computations with kinematic-hardening were carried out using a corrective scheme for the parameter $\dot{\mu}$ in each increment to ensure that the yield condition remains exactly satisfied. The increment size for the kinematic-hardening model was varied as follows: $\dot{U}/L_0 = 0.00005$ for $U/L_0 \leqslant 0.1625$ and $0.2785 \leqslant U/L_0 \leqslant 0.4785$; $\dot{U}/L_0 = 0.00008$ for $0.1625 < U/L_0 < 0.2785$ and $U/L_0 > 0.4785$. The smaller increment size corresponds to the steep parts of the load–elongation curve.

The finite-element results are shown in Figs 11–16. In these figures, solid lines refer to isotropic-hardening results, while dashed lines represent those from kinematic hardening.

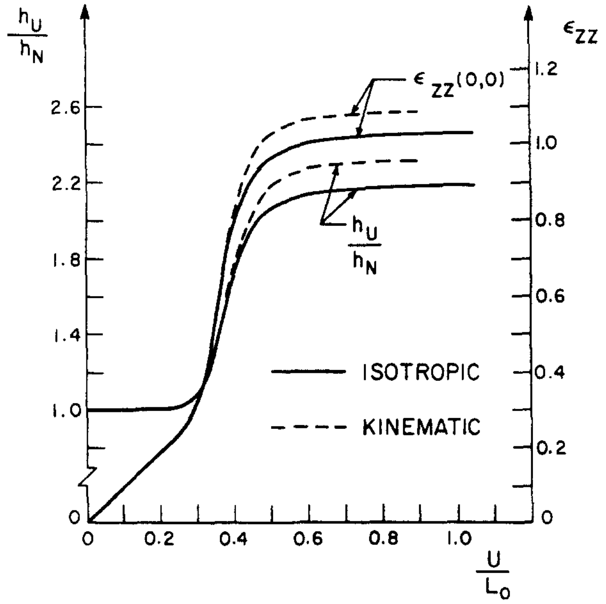

Fig. 12. Development of normalized thickness h_U/h_N at minimum section and strain $\varepsilon_{zz}(0,0)$ as a function of elongation U/L_0.

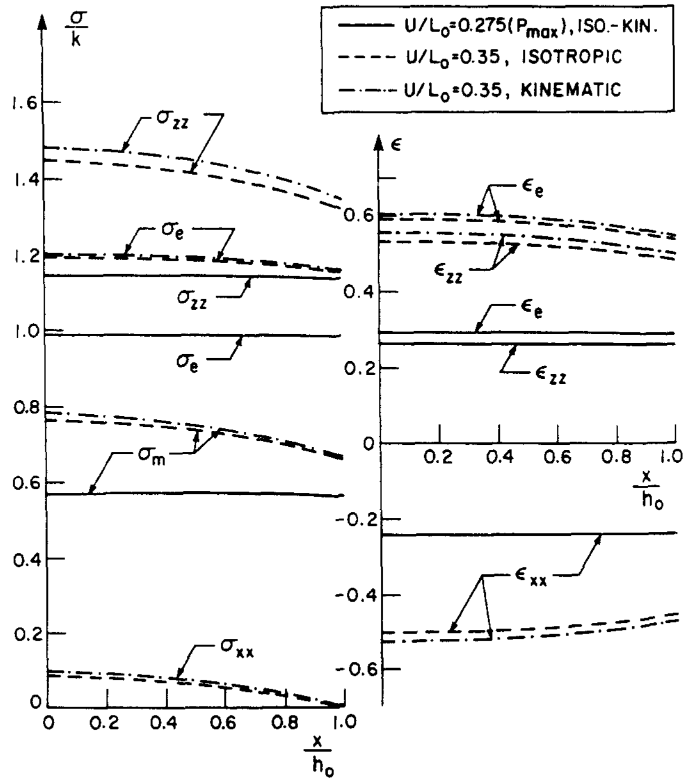

Fig. 13. Stress and strain distributions across minimum section ($z = 0$) at elongations $U/L_0 = 0.275$, 0.35.

The computed load–elongation curves for the specimen are plotted in Fig. 11. Here we observe a slight difference in the load levels at the steady-state propagation stage. Associated with this, we also find that while h_U is roughly the same for the two theories, h_N for the kinematic-hardening model is smaller than that for the isotropic-hardening one.

In Fig. 12, we show the development of the draw ratio h_U/h_N as well as $\varepsilon_{zz}(0,0)$, the corresponding physical component of logarithmic strain on the specimen axis. Neck localization for both theories is associated with the sharp transitions observed in the range

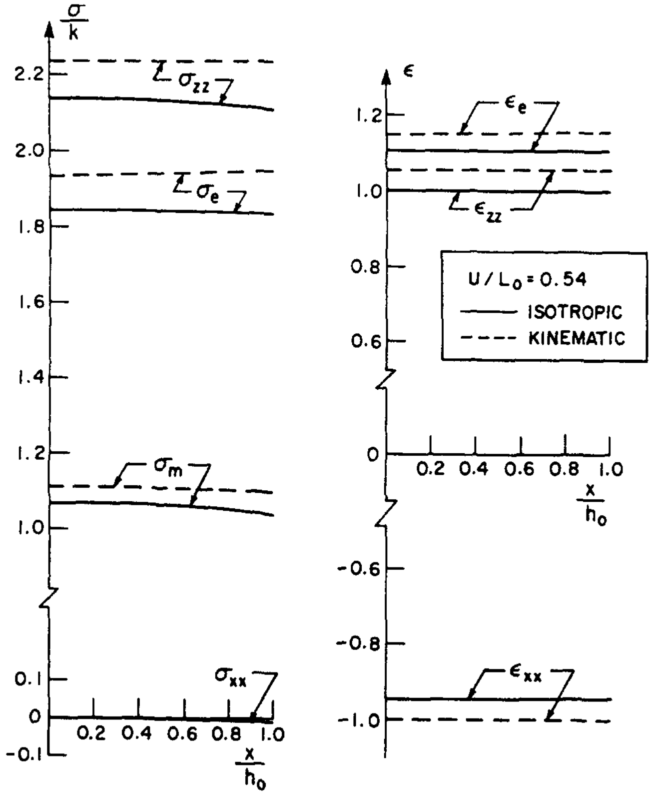

Fig. 14. Stress and strain distributions across minimum section ($z = 0$) at elongation $U/L_0 = 0.54$.

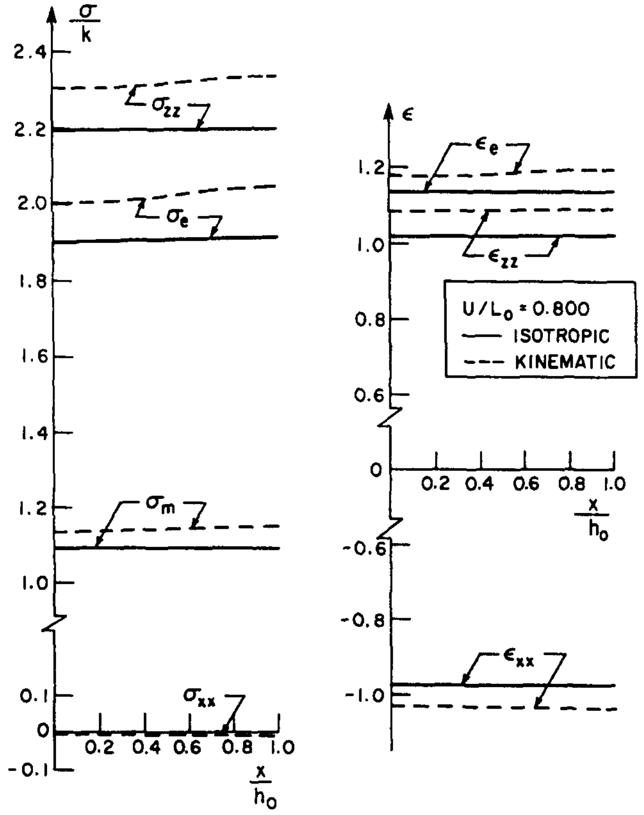

Fig. 15. Stress and strain distributions across minimum section ($z = 0$) at elongation $U/L_0 = 0.800$.

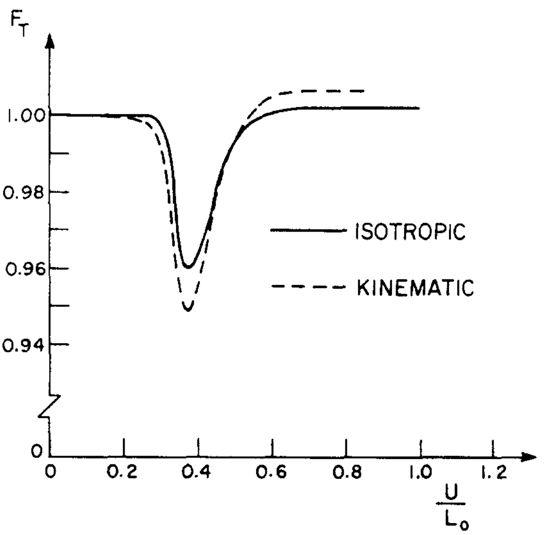

Fig. 16. Triaxiality factor $F_T = 2\bar{\sigma}_e/\sqrt{3}\,\bar{\sigma}_{zz}$ at minimum section as a function of elongation.

$U/L_0 = 0.3$–0.5. Beyond this range, necking essentially stops at the minimum section and steady-state propagation takes place along the specimen. The evolution of the stress and strain distributions at the minimum section is depicted in Figs 13–15. In these figures, σ_e is the effective true stress, as defined previously for each theory, ε_e is the effective strain as calculated from eqns (53), σ_{ij} and ε_{ij} are the physical components of true stress and logarithmic strain and $\sigma_m = \sigma_{ii}/3$ is the hydrostatic tension.

In Fig. 13, predictions for both theories at $P_{\max}(U/L_0 = 0.275)$ are essentially identical. Slight differences are observed for the distributions at $U/L_0 = 0.35$, where non-uniform stress distributions due to neck localization occur.

Results for the early stages of neck propagation are given in Fig. 14 for $U/L_0 = 0.54$. At this point, the kinematic-hardening model gives a practically uniform stress distribution across the thickness, while the isotropic-hardening model still shows stress distributions similar to those of Fig. 13.

In Fig. 15, the stress and strain distributions are compared at a well-developed stage of neck propagation $(U/L_0 = 0.80)$. In this figure, the isotropic-hardening stress distributions show practically uniform distributions across the thickness, while the kinematic-hardening stress distributions show some slight nonuniformity.

Finally, the triaxiality factors, as predicted by the two theories, are plotted in Fig. 16. The triaxiality factor for plane-strain tension is defined here as

$$F_T = \frac{2\bar{\sigma}_e}{\sqrt{3}\,\bar{\sigma}_{zz}}$$

where $\bar{\sigma}_e/\bar{\sigma}_{zz}$ is the ratio of average effective true stress to the average σ_{zz} at the minimum section and $2/\sqrt{3}$ is a normalizing factor to produce $F_T = 1$ in uniform plane-strain tension. The triaxiality factor for the plane-strain case is approximately unity at the steady-state neck propagation stage for the isotropic-hardening model. In contrast, for the axisymmetric case treated by Neale and Tuğcu (1985) the steady-state factor F_T was of the order of 1.05. The curve identified as kinematic hardening is associated with the particular definition of σ_e adopted for this model. Other definitions for σ_e, such as those implied by the Nagtegaal–de Jong or Mear–Hutchinson models, would lead to different results for F_T.

The computer time required for the finite element computations is of the order of 10^5 times that associated with the approximate two-dimensional steady-state solutions. The steady-state profiles obtained with the approximate analysis are very closely matched to the shapes obtained from the finite element calculations. A comparison between the finite element results and approximate steady-state solution shows that, as the initial geometric imperfection in the finite element solution is increased, the steady-state values for h_N/h_U

and h_U/h_0 approach those obtained from the approximate analysis. With an initial imperfection of approximately 4%, these values agree to within a few percent. A similar agreement was noted by Neale and Tuğcu (1985) for the axisymmetric case. This shows the approximate two-dimensional analysis to be an extremely efficient and quite accurate technique for analysing steady-state neck propagation phenomena in polymers.

Acknowledgements—This work was supported by the Natural Sciences and Engineering Research Council of Canada (Grants A-4479, G-1679) and le Ministère de l'Education du Québec (Programme FCAR).

REFERENCES

Coleman, B. D. (1983). Necking and drawing in polymeric fibers under tension. *Archs Ration. Mech. Analysis* **83,** 115.

Fager, L. O. and Bassani, J. L. (1984). Plane-strain neck propagation. Dept. Mech. Engng Report, University of Pennsylvania.

Hill, R. (1970). Constitutive inequalities for isotropic elastic solids under finite strain. *Proc. R. Soc.* **A314,** 457.

Hutchinson, J. W. and Neale, K. W. (1978). Sheet necking—II. Time-independent behaviour. In *Mechanics of Sheet Metal Forming* (Edited by D. P. Koistinen and N.-M. Wang). Plenum Press, New York.

Hutchinson, J. W. and Neale, K. W. (1981). Finite strain J_2 deformation theory. In *Finite Elasticity* (Edited by D. E. Carlson and R. T. Shield). Martinus Nijhoff, The Hague.

Hutchinson, J. W. and Neale, K. W. (1983). Neck propagation. *J. Mech. Phys. Solids* **31,** 405.

Mear, M. E. and Hutchinson, J. W. (1985). Influence of yield surface curvature on flow localization in dilatant plasticity. Division of Applied Sciences Report, Harvard University.

Nagtegaal, J. C. and de Jong, J. E. (1982). Some aspects of non-isotropic work hardening in finite strain plasticity. In *Plasticity of Metals at Finite Strain: Theory, Computation and Experiment* (Edited by E. H. Lee and R. L. Mallett). Stanford University.

Neale, K. W. and Tuğcu, P. (1985). Analysis of necking and neck propagation in polymeric materials. *J. Mech. Phys. Solids* **33,** 323.

Tvergaard, V. (1978). Effect of kinematic hardening on localized necking in biaxially stretched sheets. *Int. J. Mech. Sci.* **20,** 651.